The International Journal of Advanced Manufacturing Technology (2021) 114:3057–3067
https://doi.org/10.1007/s00170-021-07047-w

ORIGINAL ARTICLE

The effect of printing parameters on sintered properties of extrusion-based additively manufactured stainless steel 316L parts

Waqar Hassan[1] · Muhammad Asad Farid[1] · Anna Tosi[1] · Kedarnath Rane[1] · Matteo Strano[1]

Received: 7 October 2020 / Accepted: 5 April 2021 / Published online: 20 April 2021

Abstract

Extrusion-based additive manufacturing (EAM) is a relatively new process developed for the production of complex metallic and ceramic parts needed in smaller quantities. The debinding and sintering step of EAM is adopted from a well-known powder injection molding process. However, the 3D printing step needs special consideration to make EAM competent in the era of rapid manufacturing. This study is intended to investigate the effect of common printing parameters on the microstructure and mechanical properties of sintered stainless steel 316L (SS316L) parts manufactured through the EAM process. Part orientation (Ori), extrusion velocity (V_e), and layer height (h) were changed in experimental runs by following a full factorial design. Extrusion pressure as an indicator of melt stability and a grey relational grade as a combined response of sintered properties were analyzed against varying printing parameters. Physical characteristics measured during debinding and sintering show near isotopic shrinkage and the process is stable. Metallographic characterization in terms of porosity and grain size indicated minor differences when V_e and h were altered. Sintered parts showed improved properties when printed with vertical part orientation and $h = 0.5$ mm, whereas V_e which contributes significantly to the build-up rate was found to be responsible for melt stability. V_e at 12.5 mm/s exhibited melt stability and higher sintered properties.

Keywords Stainless steel 316L · 3D printing · Layer height · Extrusion velocity

1 Introduction

Additive manufacturing, or 3D printing, offers the prospect to create complex parts without the plan imperatives of conventional assembling courses. Additive manufacturing (AM) has been broadly engaged in the fabrication of complicated parts that are difficult to achieve through conventional machining techniques [1, 2]. The 3D printing of metals and ceramics by the extrusion of a powder/thermoplastic binder feedstock is an extrusion-based additive manufacturing (EAM) technique and has received significant interest. EAM feedstocks are generally characterized by their shear viscosity [3]. The 3D geometry of the part is sliced in a slicing program (e.g., Slic3r) and a g-code is generated. EAM feedstock is extruded and deposited according to the required path as defined through the slicing parameters [4]. The EAM process adopts the movement of an extruder, relative to a build table, to deposit thin strands (roads) of the mixture and grow a 3D object, layer by layer [5]. Another type of AM process is fused deposition modeling (FDM) where filaments of build material and support material are extruded together layer-by-layer, according to a pre-programmed trajectory. In the metal injection molding (MIM) process, feedstock is made from metallic powder and a thermoplastic-based binder is injection molded, debinded, and then finally sintered [6]. Throughout the sintering of parts that have solid loading of metallic or ceramic powders,

Highlights
- Identification of influential printing parameters for extrusion-based additively manufactured stainless steel 316L parts.
- The multi-step extrusion-based additive manufacturing (EAM) process was optimized based on extrusion pressure and grey relational grade (GRG_p) for sintered properties as the responses.
- Weight and longitudinal shrinkage show negligible changes after sintering.
- Even though there is no clear trend of GRG_P with increasing extrusion velocity (V_e). The optimal combination of considered printing parameters in EAM are V_e = 12.5 mm/s and h = 0.5 mm.

✉ Waqar Hassan
waqar.hassan@mail.polimi.it

[1] Dipartimento di Meccanica, Politecnico di Milano, Via La Masa 1, Milan, Italy

densifications take place and sintered parts show comparable properties to the bulk material [7]. Flow characteristics of feedstock govern the injection molding step as injection molding parameters particularly injection temperature and pressure are associated with the viscosity of melt [8–10]. Furthermore, control over the injection molding step is essential as defects like cracking, warpage, flow lines, weld lines in green parts, and poor mechanical strength during debinding and after sintering resulted due to inhomogeneous melt flow during the injection molding step [9, 11].

Due to the layer-by-layer process, 3D printed samples exhibit anisotropic behavior. Upright orientation shows the lowest mechanical properties. On the other hand, on-edge and flat orientation show the highest strength and stiffness [12]. However, in some AM techniques such as electron beam melting (EBM), the material may develop a fine-grained microstructure, due to multi-phase transformations prompted by a heat treatment action of the beam [13]. Also, near isotropic grains can be formed by the addition of SiC particles in a molten pool during wire and Arc additive manufacturing (WAAM) of a high-strength low alloy steel [14]. Additive manufacturing (AM), the layer-by-layer build-up of parts, has lately become an option for serial production. [15]. For large parts and due to its size limitations, it is sometimes required to join 3D printed parts with other 3D printed parts or conventionally produced parts [16]. The selective laser melting (SLM) process is of great interest for the fabrication of metal parts, and several studies have been conducted to provide an in-depth understanding of how stainless steel 316L parts can be fabricated using this powder bed fusion-based additive manufacturing (AM) process [17]. N. Chuankrerkkul deduced that the powder metallurgy method can be utilized for the manufacture of stainless steel tungsten carbide metal grid composites. The author utilized AISI 316L and tungsten carbide (WC). The stainless steel powders were blended with tungsten carbide with 5%, 10%, or 15% by weight, and compacted with 300 MPa. Higher sintering temperature led to an increase in hardness and a decrease in porosity. The most astounding value of hardness was determined from examples, containing 15 wt% of WC, sintered at 1300 °C [18].

Grade 316, second among austenitic stainless steels, is the standard molybdenum-bearing grade; excellent toughness is provided by these grades owing to the austenitic structure even down to the cryogenic temperatures [19]. The austenitic 316L stainless steel fabricated by (DLD) direct laser deposition shows a higher yield strength while keeping higher ductility than that of conventional 316L steels, mainly because the microstructure of conventional counterparts is homogeneous, while the hierarchical heterogeneous AM microstructure stimulates large plasticity eventually leading to high tensile ductility in parts fabricated by DLD [20]. However, it is a major challenge to additively manufacture metal parts with satisfactory ductility and toughness [21]. A cost-effective additive manufacturing technique known as the fused deposition of metals (FDMet) can also be used for the fabrication of 316L stainless steel parts with organic binders. Takashi Kurose et al. studied the influence of processing conditions (layer directions and layer thickness) on mechanical and shrinkage properties of the parts fabricated from the FDMet technique with a filament composed of 316L stainless steel. The highest ultimate strength of 453 MPa and strain at break of 48% were obtained in the specimens printed with a layer direction perpendicular to the tensile direction, whereas those parts which were printed parallel to the tensile direction exhibited poor mechanical properties [22].

Anne-Helene Puichaud et al. studied the effect of heat treatment (HT) and hot isostatic pressing (HIP) on the microstructure and mechanical properties of additively manufactured 316L parts. It was found that after HT, the material microstructure remains mostly unchanged, while the HIP treatment removes the material's porosity, and partially re-crystallizes the microstructure [23]. Muthukumaran and colleagues studied the corrosion and hardness behavior of AISI 316L SS implanted with argon and oxygen ions. 316L SS alloy in mill annealed condition was cut into 8-mm diameter and length of 5-mm and 15-mm size pieces. The hardness test was carried out to measure the microhardness of both the virgin and implanted specimens. The hardness profile of the surface layers was measured with various loads ranging from 10 to 100 gms. The Vickers hardness of AISI 316L stainless steel is found to be 195 Hv [24]. S316L had the lowest average hardness value of ~ 218 Hv. The hardness was improved to 273 Hv when the Pd-Ni alloy film was deposited. With the presence of W in the film, hardness values of deposited specimens saw an upward tendency. When the content of W reached up to 11.14% in the film, the hardness of the sample had the largest value ~ 343 Hv [25]. Gouda and colleagues studied the mechanical properties of tensile, compression, and bending strength of the existing material SS316L used for orthopedic implant, i.e., for femur prosthesis. According to the ASTM standards, SS316L material was purchased of dimension 16-mm diameter and machining was done according to ASTM standards; the testing for the specimens was conducted by using electronic [26]. Ala'aldin and colleagues studied the effect of building directions, infill percentage, infill patterns, print speed, extrusion temperatures, and layer height independently on mechanical properties and dimensional accuracy of FDM parts. The mechanical properties are influenced significantly by building direction, extrusion temperature, and layer height; and less significantly on infill patterns, for high infill percentages specimens, and printing speed [27].

Haijun Gong et al. studied the comparison of fabrication of metal AM parts using FDM- and SLM-based techniques [28]. It was deduced that the FDM-based method was much easier to control and less costly than the SLM-based metal AM technologies, because of the material feedstock costs and equipment needed for each operation [29]. The tensile strength and

Table 1 Chemical composition of SS 316L used as a solid loading in wt%

Element	Cr	Ni	Mo	Mn	Si	C	P	S	Fe
wt%	17.90	11.70	2.30	1.41	0.72	0.02	0.02	0.006	65.92

hardness of SLM-based metal AM process parts were higher as compared to that of FDM-based process parts [30]. M. Harraz et al. investigated that for large parts and due to its size limitations, it is sometimes required to join 3D printed parts with other 3D printed parts or conventionally produced parts. In their work, 3D printed flat plates 4 mm thick were prepared by direct laser sintering of SS316L powders. Mechanical properties and microstructure were investigated. Elongation and maximum tensile stress of 3D printed flat plates were 1.3% and 704 MPa smaller than the values 2% and 1241 MPa of cold-rolled SS316 parts [31].

A comprehensive review of relevant literature on MIM shows that the role of injection molding parameters is significant as these parameters not only correlated with the characteristics of the green part but also affects the final properties after sintering. Likewise, the process parameters controlling the 3D printing step of EAM also need to be identified and studied for the stability of the 3D printing process, part characteristics at the green and sintered state. The objective of the present study is to demonstrate the role of 3D printing parameters on melt stability during EAM and final sintered properties. The remainder of this paper is as follows: in the next section materials, 3D printing trials, post-processing, and characterization are described. Finally, the results and discussion are presented. In this paper, two synthetic responses, CV_{P_Exp} (coefficient of variation in extrusion pressure) and GRG_P (Grey Relational Grade for sintered properties) were used to assess the role of the three most common 3D printing process parameters which are part orientation (Ori), extrusion velocity (V_e), and layer height (h).

2 Materials and methods

2.1 Materials

In this study, commercially available stainless steel (SS316L) powder (make: Sandvik Osprey) was mixed with a water-soluble Embemould K83 binder. A water-soluble binder was selected because it is more environmentally friendly than other more typical options that require chemical solvents. Physical properties as specified in the SS316L powder catalog are theoretical density = 7.94 g/cm^3, average particle size D_{50} = 8.8 μm, and the chemical composition is provided in Table 1.

A feedstock having 92.5 wt% (63 vol%) solid loading of SS316L powder was obtained. The 63% by volume solid loading is the predicted region of optimal extrudability for extruded feedstocks [32]. The SEM image of SS316L feedstock is as shown in Fig. 1a. Feedstock showing binder constituents were homogeneously covered on powder particles. Before using the feedstock for extrusion-based additive manufacturing, it was characterized using a capillary rheometer for rheological properties. This SS316L feedstock was deliberately tested for a lower range of shear rates between 10 and 600 s^{-1} [3] [32], to estimate the flow behavior of feedstock during extrusion and 3D printing processes. Exponentially decreasing viscosities with shear rate is showing typical shear thinning behavior in Fig. 1b and confirms that the prepared feedstock is homogeneous and suitable for extrusion-related applications. Furthermore, the figure shows that the elongational component of viscosity is dominant at the lower shear rate due to the frictional effects of feedstock

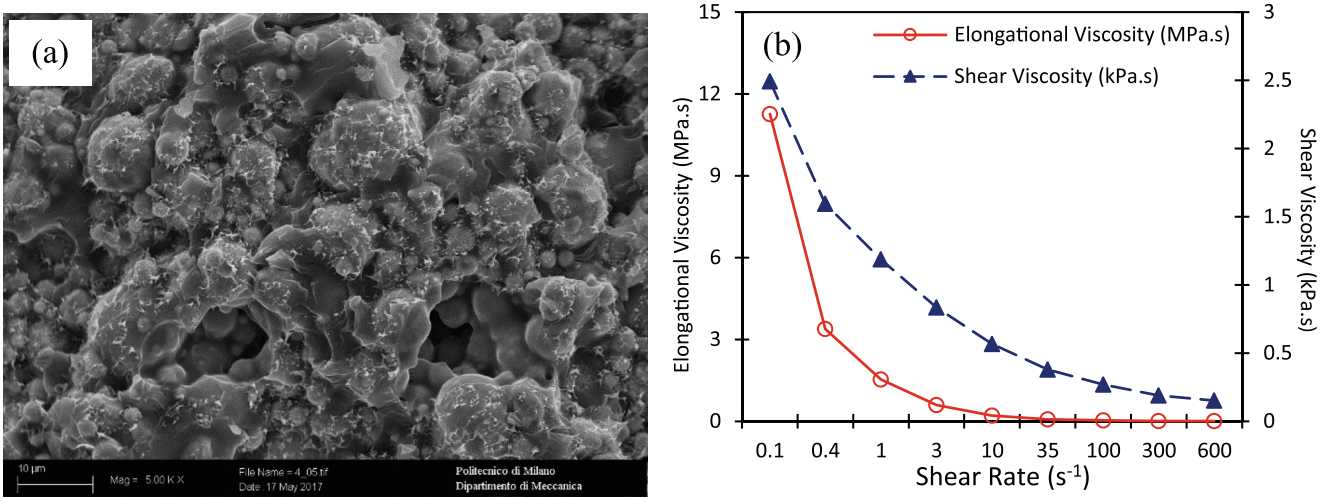

Fig. 1 Characteristics of feedstock **a** SEM image of the fractured surface of pellet and **b** viscosity components determined from the capillary test

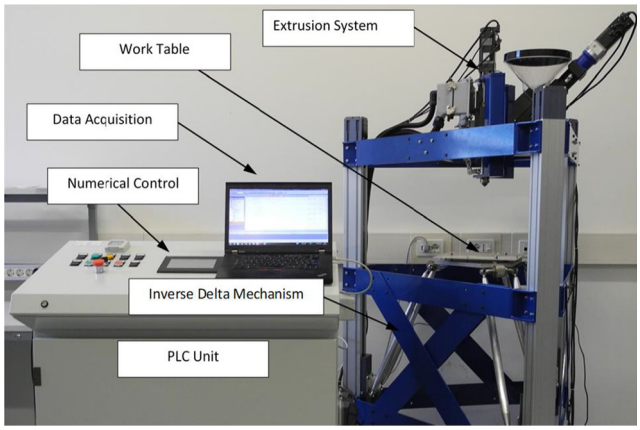

Fig. 2 Extrusion-based additive manufacturing (EFESTO), showing key elements of machine

extrusion. Thus, the shear rate of 35 s^{-1} or higher was recommended for the 3D printing step of the EAM process.

2.2 3D printing and post-processing

A specially developed machine, EFeSTO (extrusion of feedstock for the manufacturing of sintered tiny objects), available at Politecnico di Milano, Italy, was used for 3D printing of SS316L feedstock. The main features of the EFeSTO machine are a parallel-kinematics linear delta system for 3D movement of deposition plate and a fixed heavy-duty extruder system for deposition of high powder loaded polymeric mixture [3]. Figure 2 shows the parallel kinematics machine that constitutes the 3D printer. This design is equipped with three rigid links connected to the moveable platform to one side and a linear guide on the other side [33].

In this study, rectangular (60 mm × 10 mm × 6 mm) bar-shaped parts were 3D printed in two-part orientations: horizontal (*H*), laying on the face of dimensions 60 mm × 10 mm as shown in Fig. 3(a) and vertical (*V*), laying on the face of dimensions 60 mm × 6 mm as shown in Fig. 3(b).

Previous work [34–36] shows that dimensional control and build-up rate (bur) can be improved simultaneously when higher solid loading (63 vol%), lower extrusion temperature (T_e < 150 °C), V_t/V_e < 1, and lower shear rate below 500 s^{-1} are used. Furthermore, table velocity (V_t) and hatch spacing are less significant parameters. Printing parameters such as extrusion temperature (T_e) and nozzle diameter (D_n) were kept constant at 135°C and 0.8 mm respectively. Whereas, extrusion velocity (V_e), layer height (h), and part orientation were varied at different levels as given in Table 2. The focus of this work is towards the mechanical strength of the 3D printed stainless 316L parts; because of this, the outer shell of the 3D printed part (perimeter) which is accountable for the surface quality of the parts is neglected and rectilinear infill path with the angle of 45^0 is considered as shown in Fig. 3. A total of 54 samples were produced based on 18 experimental conditions with three replicates from this full factorial design. For each 3D printing test, extrusion pressure (P_i) was collected at intervals of 50 s throughout the tests. Individual samples of the pressure readings is P_{Exp} (MPa), the average total pressure (μ_P) of was calculated along with the standard deviation (σ_P). 3D printed samples are termed as green parts.

Green parts were firstly measured for weight and dimensions and then solvent debinded in a bath of agitated water, maintained at 40 °C. Solvent debinding was performed for 48 h to ensure maximum removal of sacrificial binder from the parts. After solvent debinding, parts were dried completely to ensure the complete removal of moisture from the parts. During thermal debinding, parts were heated in an oven at a heating rate of 20 °C/h up to a temperature of 145 °C with 4-h hold time and then at a heating rate of 10 °C/h up to a temperature of 300 °C with 2-h hold time, followed by natural cooling in the oven. Weights of parts after each debinding step were measured to confirm the complete removal of binder constituents during these intermediate steps. Finally, parts were sintered in inert gas (argon gas) atmosphere at a temperature of 1350 °C for 1 h. The sintering cycle consists of a heating rate of 130 °C/h up to a sintering temperature of 1350 °C, holding for 1 h at 1350 °C, and then furnace cooling. Near isotropic shrinkage after sintering is realized from Fig. 4 wherein the part orientation is also compared.

2.3 Characterization of 3D printed parts

Part characteristics during solvent debinding, thermal debinding, and sintering were studied based on weight change after each step with respect to the weight of part at the green step, whereas sintered parts were used for non-destructive as well as destructive measurements. The density of the sintered

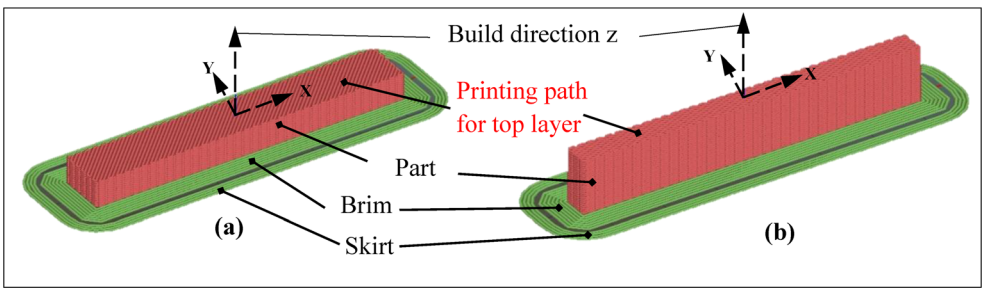

Fig. 3 CAD representation of parts 3D printed with (**a**) horizontal part orientation and (**b**) vertical part orientation

Table 2 Printing parameters and their levels considered in this full factorial experimental design

Parameters	Levels	
	Horizontal (*H*)	Vertical (*V*)
Orientation, Ori		
Extrusion velocity, V_e (mm/s)	7.5	12.5 17.5
Layer height, *h* (mm)	0.3	0.4 0.5

parts was measured using Archimedes' principle. Longitudinal shrinkage (%) was calculated by measuring the dimensions of each part in green state and after sintering. Considering the selected printed strategy, i.e., without perimeter the surface of the sintered part, is rough. So, to have a smooth surface finish for mechanical testing, all the samples were polished. For microscopic studies, firstly samples were prepared by buffing and chemical etching. A scanning electron microscope (Zeiss EVO 50XVP SEM) equipped with a backscattered electron detector (BSE) was used for capturing micrographs. Porosity analysis was carried out on images before etching whereas analysis of grain size and distribution after chemical etching. Metallographic analysis in terms of porosity and grain size was carried out using ImageJ software. To measure the hardness, the rectangular shape sintered specimens were polished to have a mirror-like surface. Microhardness (HV) was measured using a hardness tester (FM-810, make: Future Tech). Each part was indented at three points on three faces top, bottom, and side, with a 100 g load and 15-s dwell time setting. Both average and standard deviation were calculated and used for analysis. Likewise, flexural strength (σ_f) was calculated from the 3-point bending test. MTS RT/150 machine with a rated force capability of 150kN was used for the purpose. ASTM A370-18 standard was followed for testing. The values of crosshead position (mm) and deflections (mm) with high accuracy were provided by the deflectometer. The crosshead speed was set to 2 mm/min for all mechanical tests. The elastic modulus (*E*) of each specimen was evaluated by approximating their engineering stress-strain plot to the linear regression model. A couple of green and sintered parts were tested for assessing surface characteristics (top, bottom, and side) using Alicona Infinite Focus microscope.

3 Results and discussion

3.1 Physical and microstructural characteristics

As extrusion-based additive manufacturing (EAM) is a multi-step process, the completion of intermediate steps may influence the sintered properties of parts [4, 7]. The weight change through the intermediate steps was assessed with respect to the weight of the green part. Figure 5 shows the results of the weight change (ΔW %) after intermediate process steps (solvent debinding, thermal debinding, and sintering). The effect of V_e on ΔW was found to be negligible. The average ΔW after solvent debinding is about 3.46%; similarly, ΔW after thermal debinding and sintering is 6.54% and 7.63% respectively. The theoretical ΔW given in the specification of the binder after sintering is 7.50%. The marginal difference of 0.13% between as observed and theoretical ΔW is due to material removal while handling of parts during intermediate steps. After sintering parts were characterized for sintered density and overall density was reported as 7.11 ± 0.13 g/cm^3.

An overall longitudinal shrinkage of 12.7% was observed in SS316L parts after sintering. Figure 6 shows a marginal increase in linear shrinkage (ΔL/L %) for each increment of the V_e and *h* level. This marginal variation in (ΔL/L %) was due to an apparent difference in the packing of the deposited roads during 3D printing. It is worth noting that with further increase in the level of V_e and *h* beyond 17.5 mm/s and 0.5 mm, the green parts were not dimensionally stable and hence eliminated from these experimental studies. Based on Figs. 5 and 6, it is established that the physical changes during EAM steps have a negligible influence on 3D printing parameters. The completion of intermediate steps or dimensional stability of sintered parts was directly correlated to the part characteristics at the green step [7].

The microstructure of sintered SS316L parts is shown in Fig. 7. The pores and grain boundaries in sintered parts are visible and marked in the microstructure. The effect of extrusion velocity on porosity and grain characteristics cannot be visibly distinguished from these (Fig. 7(a), (b), (c)) micrographs. The elemental mapping was carried out at locations A, B, and C as marked in Fig. 7(d). At the grain boundaries

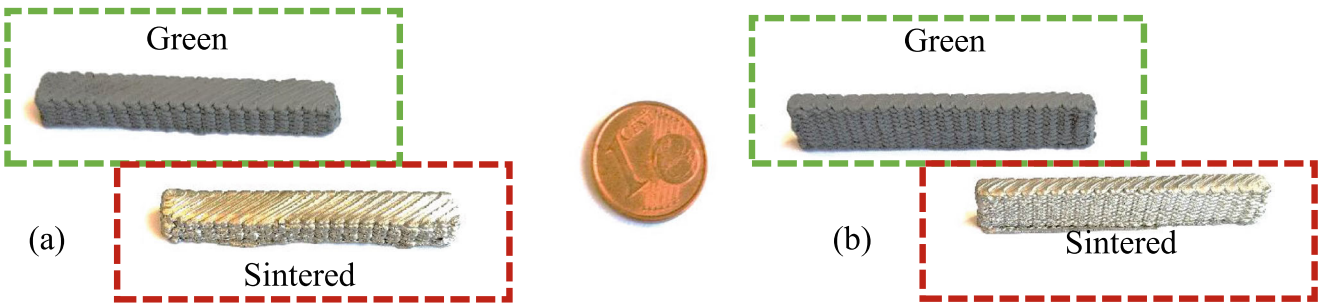

Fig. 4 SS316L parts printed with **a** horizontal and **b** vertical orientation at the green and sintered state

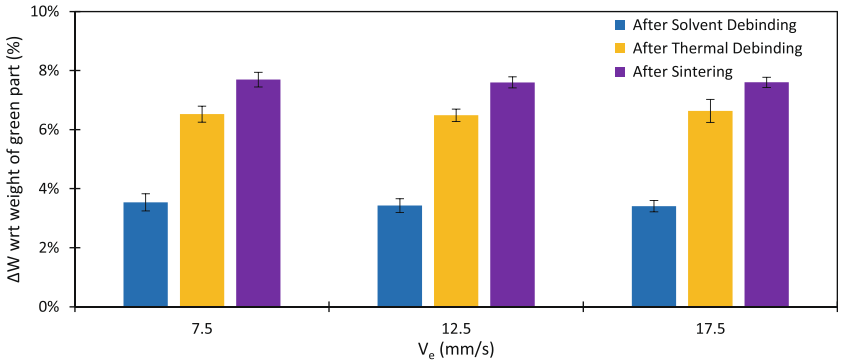

Fig. 5 The effect of extrusion velocity on weight change during EAM of SS316L parts

(positions A and B), the carbon content is marginally higher as compared to in the grain (position C); this may be due to the formation of carbide as chromium content is also marginally depleted at the grain boundaries.

The porosity in metal AM parts is generally not desirable as it reduces strength. It might be reduced with further post-processing treatments like HIP (hot isostatic pressing) [23]. A longer sintering time would not help in the present case, since it would lead to an increase in grain size. Some precipitates are inside the grains according to Fig. 7, but pores are on grain boundaries.

Furthermore, the metallographic analysis was carried out using the ImageJ tool to investigate and quantify the role of printing parameters on the microstructure of sintered parts. The porosity is described by empty (black) spaces in the micrograph and was calculated by a ratio of the area of empty spaces to the overall area of the micrograph. Similarly, the average grain size was calculated through the linear intercept method as defined in ASTM E112-13 [37, 38]. Tables 3 and 4 show how the porosity and average grain size change with V_e and h in sintered SS316L parts.

The porosity (%) of sintered parts increases marginally with the increase in V_e, whereas there is a nonlinear trend in porosity with increasing h. Indeed, it is reasonable that when the layer height is too high (beyond 0.5 mm), the porosity increased because of a more difficult packing of the layers and roads. Conversely, when the layer height is too small, porosity might also increase again because the number of roads increases and therefore there is a larger number of interface surfaces between roads with a greater probability of inefficient packing. V_e seems to have an increasing trend for the average grain size, whereas change in h is showing an unclear trend for the grain size as well. The minor increasing trend of the porosity and grain size with V_e can be interpreted with the change in deposited road placing and particle packing during 3D printing.

3.2 Mechanical characteristics of sintered parts

Sintered samples were also used for mechanical characterization, particularly, hardness, flexural strength, and elastic modulus. A microhardness test was carried out using an FM-180 hardness tester and Vicker's pyramid number (HV) was

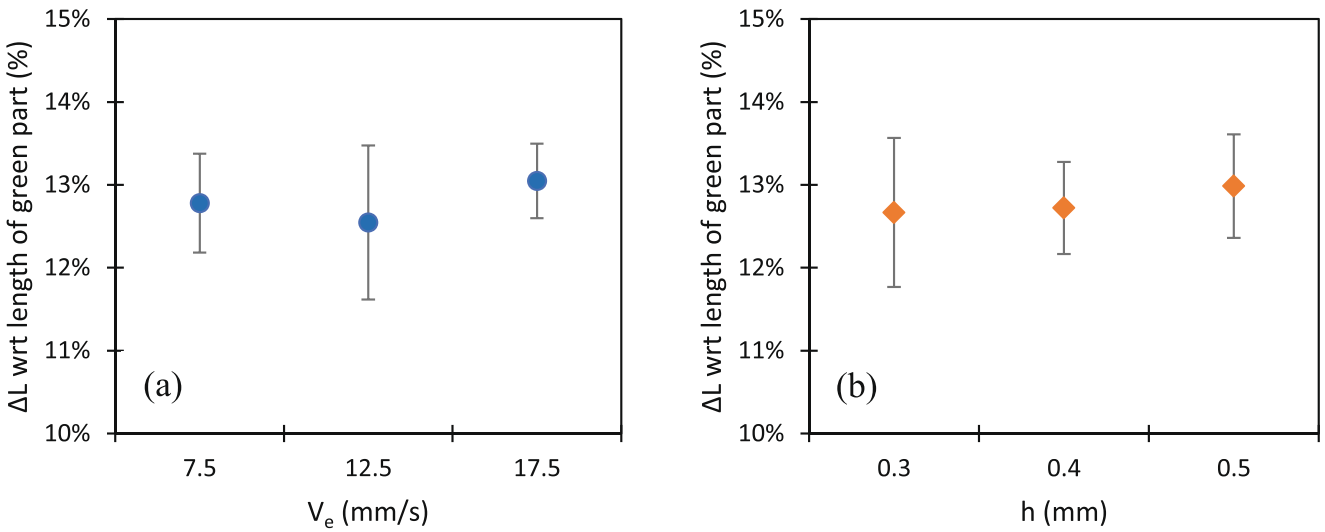

Fig. 6 The role of 3D printing parameters **a** V_e and **b** h on dimensional changes after the sintering step

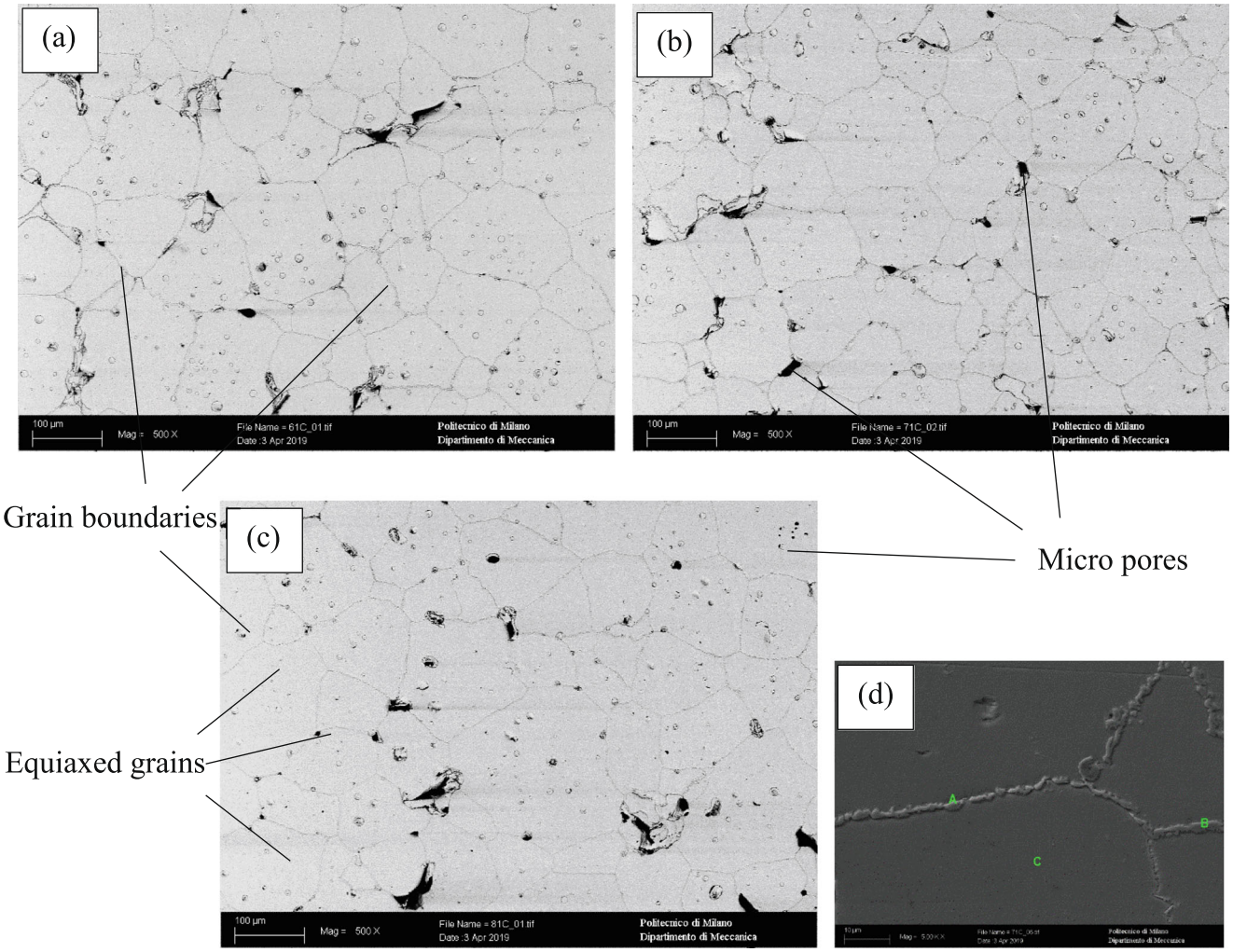

Fig. 7 SEM micrographs of sintered SS316L parts at different V_e (**a**) 7.5 mm/s, (**b**) 12.5 mm/s, (**c**) 17.5 mm/s, and (**d**) elemental analysis

reported. The flexural strength (σ_f) and elastic modulus (E) was calculated from the 3-point bending tests. The flexural strength of the part was calculated using Eq. (1).

$$\sigma_f = \frac{3FL}{2bt^2} \tag{1}$$

where σ_f = flexural strength or modulus of rupture (MPa), F = maximum force at rupture (kN), $L = (2r + 3t)$ span length (mm), b = width (mm), and t = thickness (mm) of the part.

The elastic modulus (E) of each part was evaluated by approximating their engineering stress-strain plot to a linear regression model. The representative engineering stress-strain curves of parts produced with horizontal and vertical orientation are shown in Fig. 8.

A similar flow curve was observed in both Fig. 8a and b for horizontal and vertical part orientation specimens. A negligible variation was found when flow curves were compared for different V_e, whereas parts with different layer height (h) show significant variation in flow curve if plotted at a constant V_e. Parts printed with h = 0.5 mm shows higher strain hardening as compared to parts manufactured with h = 0.3 and 0.4 mm. Previous studies reported that the number of layers and discontinuities in the samples are lower when layer height (h) is higher which also improves the strength of the parts [27].

3.3 Role of printing parameters on CV_{P_Exp} and GRG_P

Mean (μ_P) and standard deviation (σ_P) of extrusion pressure P_{Exp} (MPa) were acquired during each 3D printing trial. To check the effect of printing parameters on extrusion pressure, a response CV_{P_Exp} (coefficient of variation in extrusion

Table 3 The effect of extrusion velocity V_e (mm/s) on the metallographic characteristics of sintered SS316L parts

V_e (mm/s)	h (mm)	Porosity (%)	Grain size (µm)
7.5	0.5	3.88	81.44
12.5	0.5	4.12	88.51
17.5	0.5	4.34	90.84

Table 4 The effect of layer height h (mm) on the metallographic characteristics of sintered SS316L parts

V_e (mm/s)	h (mm)	Porosity (%)	Grain size (μm)
12.5	0.3	3.62	10.24
12.5	0.4	2.32	9.93
12.5	0.5	4.12	10.7

pressure) during 3D printing was calculated using Eq. (2). CV_{P_Exp} can be useful for assessing the stability of melt during the 3D printing process [3].

$$CV_{P\_Exp} = \frac{\sigma_P}{\mu_P} \quad (2)$$

where σ_P and μ_P are the standard deviation and mean of extrusion pressure respectively.

Instead of discussing the effect of printing parameters on individual properties of sintered parts, namely sintered density (ρ), hardness (HV), flexural strength (σ_f), and elastic modulus (E), a variable grey relational grade for properties (GRG_P) was established. Firstly, all the properties were normalized and grey relational coefficients (GRC_{Pi}) were determined. Grey relational grade (GRG_P) was established by considering equal weightage to grey relational coefficients. A standard grey relation formula was implemented to calculate the above said GRC_{Pi} and GRG_P, hence the optimal parameters combination was determined which shows the highest GRG_P [39–42]. The multi-way ANOVA was performed at a 90% confidence interval for CV_{P_Exp} and GRG_P. Interval plots as given in Fig. 9 show the variation in CV_{P_Exp} and GRG_P with respect to printing parameters.

It seems that there was an insignificant variation in CV_{P_Exp} if part orientation was altered. The vertical part orientation samples had marginally higher GRG_P values as compared to the horizontal counterparts. CV_{P_Exp} for parts manufactured with h = 0.3 mm is significantly higher due to the squeezing action of melt [3, 27]. Moreover, it is clear from Fig. 9d that for both part orientations (horizontal and vertical) at h = 0.5-mm parts have higher GRG_P values, which indicates that with the increase in the layer height, the sintered properties were significantly improved. The reason for improved sintered properties was discussed earlier in the context of flexural strength which is equally applicable for the rest of the properties [27].

The plot in Fig. 9e shows that with increasing V_e the CV_{P_Exp} significantly dropped. This behavior of extrusion pressure was connected with the rheological effect of melt. With increasing V_e, the strain rate increases, and viscosity decreases as shown in Fig. 1b. Thus, V_e = 12.5 or higher gives a stable melt extrusion regime. Figure 9f shows that the GRG_P value was higher at 12.5 mm/s extrusion velocity; however, no clear trend was observed for GRG_P with respect to V_e and it was not a significant factor as indicated by ANOVA. Based on this multi-objective optimization exercise, the melt stability during 3D printing and sintered properties can be simultaneously improved when V_e is set at 12.5 mm/s and h is set at 0.5 mm.

Table 5 shows the surface roughness of the 3D printed cube-shaped part for which perimeter was considered along with 100% infill. The surface profile of sintered part is different from the green part. Each side of the cuboid part (top, side, and bottom) shows a smooth surface after sintering. The green part shows higher surface roughness on the sides because of the layer-by-layer addition, while the surface roughness is higher on the top than the bottom due to the deposition of the material. The bottom of the part has less surface roughness because it touches the flat build platform. The same trend also follows in sintered part.

4 Conclusion

This study reports the effect of 3D printing parameters on extrusion-based additive manufactured parts. An extrusion-

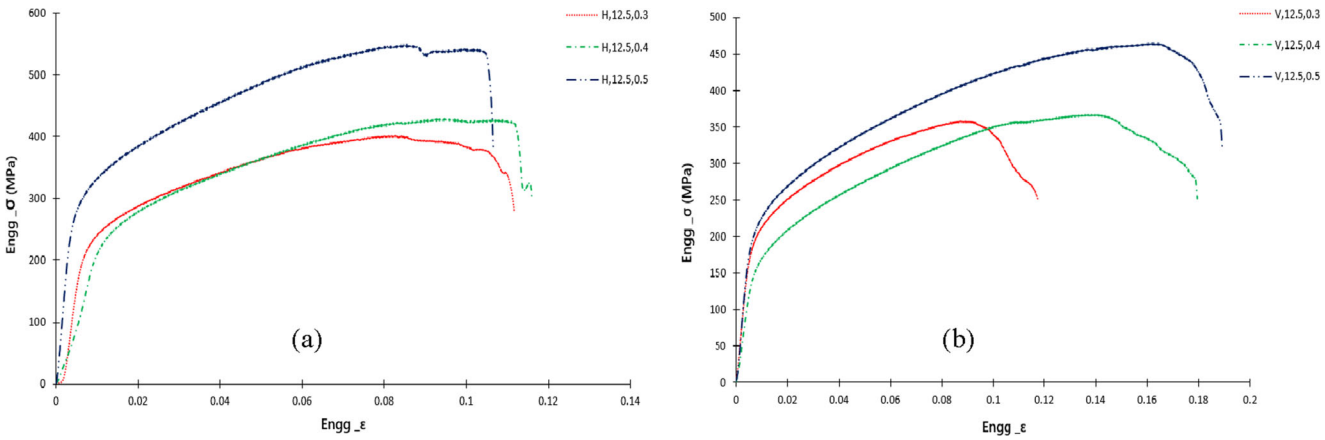

Fig. 8 Engineering stress-strain curves of horizontally and vertically printed SS316L parts. **a** Horizontal part orientation, **b** Vertical part orientation

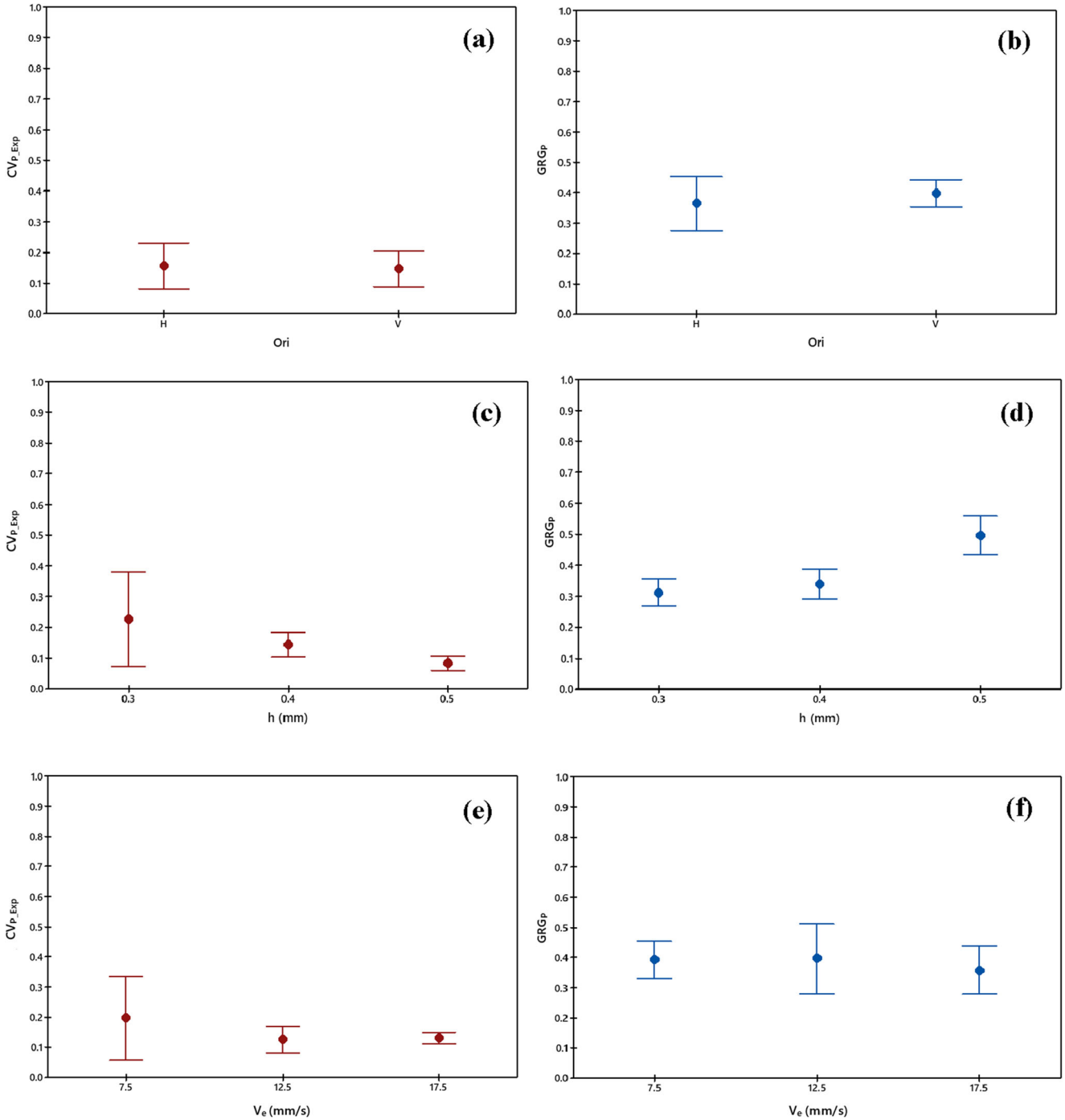

Fig. 9 Interval plots for CV_{P_Exp} and GRG_P with respect to Ori (**a**, **b**), h (**c**, **d**), and V_e (**e**, **f**) respectively

based additive manufacturing (EAM) technique was recently identified as a cost-efficient and rapid production process for metallic and ceramic objects because of the unique features of enabling methods fused deposition modeling (FDM) and powder injection molding (PIM). Taking advantage of SS 316L feedstock extrusion [5], and experimental trials were carried out by varying three printing parameters and multiple rectangular bars were manufactured. During 3D printing, extrusion pressure was recorded and further treated for evaluating melt stability during the process. Physical and mechanical properties were measured like sintered density, hardness, flexural strength, and elastic modulus. Based on observations discussed in Section 3, the following conclusions were recognized,

1) The weight change in EAM parts was increased with the progression of the debinding steps due to the removal of binders. The average weight change after solvent

Table 5 Surface roughness (μm) of part during EAM processing

Green	Part condition	Sintered
6.97	Top	5.68
11.42	Side	7.14
3.75	Bottom	1.92

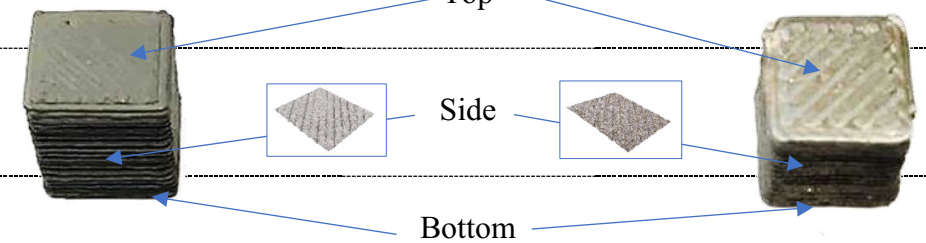

debinding was ~3.46%, after thermal debinding was ~6.54%, and negligible after sintering. The longitudinal shrinkage for SS316L exhibited negligible variation against increasing V_e and h. Thus, post-processing stages are found to be stable irrespective of 3D printing parameter settings.

2) The porosity in sintered SS316L parts showed an increasing trend with the increase in extrusion velocity whereas no trend was observed with increasing layer height. Similarly, an increasing trend between grain size and extrusion velocity was observed because of the change in deposited road placing and particle packing during 3D printing. The average grain size at the center was larger as compared to the outer edge because of the variable densification in the part during the sintering phase.
3) Extrusion velocity was the most influential parameter for improving melt stability based on ANOVA analysis on CV_{P_Exp} and with increasing V_e, strain rate and melt stability increase as the role of elongational viscosity is dominant at a lower shear rate, whereas a compound response GRG_P for sintered properties was considered. Based on ANOVA analysis, the ascending trend of influential 3D printing parameter is: part orientation-extrusion velocity-layer height.
4) If individual properties were considered, the flexural strength of the part built-in horizontal orientation was found to be higher than those of vertical orientation. The crack initiated along the thickness of vertical parts increased the chances of failure at a lower level of deflection during a 3-point bending test. Within the same orientation and keeping the extrusion velocity constant, specimens showed the highest flexural strength values for layer height = 0.5 mm due to limited discontinuities in the part.
5) Even though there is no clear trend of GRG_P with increasing V_e, the optimal combinations of considered printing parameters in EAM are V_e = 12.5 mm/s and h = 0.5 mm.

Acronyms *PIM/MIM* , powder/metal injection molding; *AM,* additive manufacturing; *FDM,* fused deposition modeling; *EAM,* extrusion-based additive manufacturing; *FDMet* , fused deposition of metals; *DLD,* direct laser deposition; *SLM,* selective laser melting; D_n, nozzle diameter; V_e, extrusion velocity; V_t, table velocity; $Engg\_\varepsilon$, engineering strain; $Engg\_\sigma$, engineering stress; σ_f , flexural strength/modulus of rupture; h, layer height; *Ori,* part orientation; ρ, density; *E,* elastic modulus; *HV,* Vickers's hardness number; *H,* horizontal orientation; *V,* vertical orientation; CV_{P_Exp}, coefficient of variation for extrusion pressure; GRG_P, grade relational grade for sintered properties

Author contribution Waqar Hassan: conceptualization, methodology, software, and writing-original draft. Muhammad Asad Farid: resources, visualization, experimentation, and investigation. Anna Tosi: resources and investigation. Kedarnath Rane: resources, visualization, and investigation. Matteo Strano: formal analysis, supervision, and writing-review & editing.

Data availability Not applicable.

Declarations

Ethics approval and consent to participate Not applicable. This manuscript does not contain any studies with human participants or animals performed by any of the authors.

Consent for publication Not applicable.

Competing interests The authors declare no competing interests.

References

1. Oliveira TSRMJP (2020) Revisiting fundamental welding concepts to improve additive manufacturing: From theory to practice. Prog Mater Sci 107:100590
2. Oliveira ALJMJP (2020) Processing parameters in laser powder bed fusion metal additive manufacturing. Mater Des 193:108762
3. Rane TB a MSK (2020) Role of elongational viscosity of feedstock in extrusion-based additive manufacturing of powder-binder mixtures. Int J Adv Manuf Technol 107(11):4389–4402

4. Kedarnath Rane SPMS (2020) Evolution of porosity and geometrical quality through the ceramic extrusion additive manufacturing process stages. Addit Manuf 32:101038
5. Kedarnath Rane LM (2019) Processability of SS316L powder - binder mixtures for vertical extrusion and deposition on table tests. Powder Technol 345:553–562
6. Rane K, Date P (2020) A dimensional analysis based model to predict completion of solvent debinding step for Metal Injection Moulded parts. Adv Mater Process Technol:1–21
7. Rane K, Date P (2019) Evolution of properties of parts during MIM and sintering of recycled oxide particles. Powder Metall 62(2):133–145
8. Karatas AKHUSSC (2004) Rheological properties of feedstocks prepared with steatite powder and polyethylene-based thermoplastic binders. J Mater Process Technol 152:77–83
9. Rane KK, Date P (2014) Rheological investigation of MIM feedstocks for reducing frictional effects during injection moulding. Adv Mat Res 966–967:196–205
10. P &. Pachauri HM (2015) Optimization of injection moulding process parameters in MIM for impact toughness of sintered parts. Int J Adv Mater Metall Eng 1(1):1–11
11. J. C. B. T &. Gelin SJ (2010) Processing defects and resulting mechanical properties after metal injection molding. J Eng Mater Technol 132(1)011017
12. Chacóna MEG-PPNJM (2017) Additive manufacturing of PLA structures using fused deposition modelling: Effect of process parameters on mechanical properties and their optimal selection. Mater Des 124:143–157
13. F. B. M. D. W. O. V. H. B &. Günther TNJ (2018) Design of novel materials for additive manufacturing - Isotropic microstructure and high defect tolerance. Sci Rep 8(1):1–14
14. Tiago VDDTJAAJEERNSTGSJO, Rodrigues A (2020) In-situ strengthening of a high strength low alloy steel during Wire and Arc Additive Manufacturing (WAAM). Addit Manuf 34:101200
15. Herzog D, Seyda V, Wycisk E, C.E (2016) Additive manufacturing of metals. Acta Mater 117:371–391
16. Harraz M, El-Mahallawy N, Abd Elghany K, Schleser M, Palkowski H, Klinger A (2017) Characterization of 3D Printed Stainless Steel SS316L Powders Joined by TIG, Plasma and Laser Welding. J Eng Sci Mil Technol 1(2):91–95
17. Gong H, Snelling D, Kardel K, Carrano A (2019) Comparison of Stainless Steel 316L Parts Made by FDM-and SLM-Based Additive Manufacturing Processes. JOM 71(3):880–885
18. Chuankrerkkul N, Lorchaiyanunt C, Tansittipan S, Polsilapa S (2009) Powder metallurgy of stainless steel - tungsten carbide composites. In: ICCM-17
19. AZoM (2004) "Azo Material," 18 Feb 2004. [Online]. Available: https://www.azom.com/article.aspx?ArticleID=2382. Accessed 16 Apr 2019
20. P. A. P. H.-A, Barkia TALGFSHMB (2019) On the origin of the high tensile strength and ductility of additively manufactured 316L stainless steel: multiscale investigation. Mater Sci Technol 41:209–218
21. Zhongji Sun XSBTACKC (2018) Simultaneously enhanced strength and ductility for 3D-printed stainless steel 316L by selective laser melting. NPG Asia Mater 10:127–136
22. Kurose T, Abe Y, Santos MVA, Kanaya Y, Ishigami A, Tanaka S, Ito H (2020) Influence of the Layer Directions on the Properties of 316L Stainless Steel Parts Fabricated through Fused Deposition of Metals. Materials 13(11):2493
23. Puichaud Anne-Helene CFACFLERP-FGHMFSAJ-LB (2019) Microstructure and mechanical properties relationship of additively manufactured 316L stainless steel by selective laser melting. EPJ Nucl Sci Technol 5:23
24. Muthukumaran V, Selladurai V, Nandhakumar S, Senthilkumar M (2009) Corrosion and Hardness Behaviour of AISI 316L SS Implanted with Argon and Oxygen Ions. Manuf Eng 9(2):75–79
25. Zhang Z, Tang J, Wang Y, Preutesei M, Wang H (2017) Electrodeposition of A Novel Pd-Ni-W Ternary Alloy Film on SS316L. Int J Electrochem Sci 12:6180–6189
26. Gouda SPJ, D.A.T., Dinesh KR, Prashanth N, Hatapaki N (2014) Evaluation of mechanical properties of existing material SS316L used as femur bone implant material. Int J Innov Res Technol Sci 2:52–58
27. Alafaghani A, Qattawi A, Alrawi B, Guzman A (2017) Experimental Optimization of Fused Deposition Modelling Processing Parameters: a Design-for-Manufacturing Approach. Procedia Manuf 10:791–803
28. Lopes CMMVRDTARTGSJPOJG (2020) Effect of milling parameters on HSLA steel parts produced by Wire and Arc Additive Manufacturing (WAAM). J Manuf Process 59:739–749
29. Lopes CMMVRDTARTGSJPOJG (2020) Effect of milling parameters on HSLA steel parts produced by Wire and Arc Additive Manufacturing (WAAM). J Manuf Process 59:739–749
30. Gong H, Snelling D, Kardel K, Carrano A (2019) Comparison of Stainless Steel 316L Parts Made by FDM-and SLM-Based Additive Manufacturing Processes. Jom 71(3):880–885
31. Haraz M, El-Mahallawy N, Schleser M, Abd Elghany K, Palkowski H, Klingner A (2017) Characterization of 3D Printed Stainless Steel SS316L Powders Joined by TIG-, Plasma- and Laser. Journal of Engineering Science and Military Technologies 1(2):91–95
32. Matteo Strano KRFBVLDL (2019) Extrusion of metal powder-polymer mixtures: Melt rheology and process stability. J Mater Process Technol 273:116250
33. Hermes Giberti MSAMA (2016) An innovative machine for Fused Deposition Modeling of metals and advanced ceramics. In: MATEC web of conferences
34. Kedarnath Rane KCMS (2019) Rapid surface quality assessment of green 3D printed metal-binder parts. J Manuf Process 38:290–297
35. Strano KRFBVLDLM (2019) Extrusion of metal powder-polymer mixtures: Melt rheology and process stability. J Mater Process Tech 273:116250
36. Kedarnath Rane LDLMS (2019) Processability of SS316L powder - binder mixtures for vertical extrusion and deposition on table tests. Powder Technol 345:553–562
37. Lixin XZWSRXWMZ (2016) Grain Size Automatic Determination for 7050 Al Alloy Based on a Fuzzy Logic Method. Rare Metal Mater Eng 45(3):548–554
38. Pauli Lehto HRTSHHJR (2014) Influence of grain size distribution on the Hall–Petch relationship of welded structural steel. Mater Sci Eng A 592:28–39
39. Ulas Caydas AH (2008) Use of the grey relational analysis to determine optimum laser cutting parameters with multi-performance characteristics. Opt Laser Technol 40:987–994
40. Prashant CP, Patil J (2016) Analysis of process parameters in surface grinding using single objective Taguchi and multi-objective grey relational grade. Perspect Sci 8:367–369
41. Nitesh Kumar Dixit RSRN (2016) Comparison of Two Different Rapid Prototyping System based on Dimensional Performance using Grey Relational Grade Method. Procedia Technol 25:908–915
42. Prakash JMKSKS (2015) Optimization of drilling characteristics using Grey Relational Analysis (GRA) in Medium Density Fiber Board (MDF). Mater Today 2:1541–1551